

Robust Unmixing of Multitemporal Hyperspectral Images

Pierre-Antoine Thouvenin, *Student Member, IEEE*, Nicolas Dobigeon, *Senior Member, IEEE* and Jean-Yves Tourneret, *Senior Member, IEEE*

Abstract—We propose a mixture model accounting for smooth temporal variations, construed as spectral variability, and abrupt changes interpreted as outliers. The resulting unmixing problem is tackled from a Bayesian point-of-view, and the inference is conducted using a Markov chain Monte Carlo (MCMC) method to assess the flexibility of the proposed approach. A comparison with unmixing techniques from the literature on synthetic and real data finally allows the interest of the proposed approach to be appreciated.

Index Terms—Hyperspectral imagery, multitemporal images, endmember variability, Markov chain Monte-Carlo (MCMC) methods.

I. INTRODUCTION

ACQUIRED in hundreds of contiguous spectral bands, hyperspectral (HS) images have known an increasing interest due to the significant spectral information they convey, which is somewhat mitigated by their lower spatial resolution in specific applications (such as remote sensing). This limitation, combined with possibly complex interactions between the incident light and the observed materials, implies that the observed spectra are mixtures of several signatures corresponding to distinct materials. Spectral unmixing then consists in identifying a limited number of reference spectral signatures composing the data – referred to as *endmembers* – and their abundance fractions in each pixel according to a predefined mixture model. The choice of a specific model generally reflects the practitioners’ prior knowledge on the environmental factors possibly affecting the acquisitions, such as declivity or multiple reflections. Traditionally, a linear mixing model (LMM) is adopted since it is appropriate to describe hyperspectral data when the declivity of the scene and microscopic interactions between the observed materials are negligible [1]. However, varying acquisition conditions, such as local illumination variations or the natural evolution of the scene, may significantly alter the shape and the amplitude of the acquired signatures [2], [3], thus affecting the extracted endmembers. While endmember variability has hitherto been extensively considered within a single HS image, either in a deterministic [4]–[7] or a statistical setting [8]–[10], fewer

This work was supported in part by the Hypanema ANR Project no. ANR-12-BS03-003, by the MapInvPlnt ERA-NET MED Project no. ANR-15-NMED-0002-02, by the Thematic Trimester on Image Processing of the CIMI Labex under Grant ANR-11-LABX-0040-CIMI within the Program ANR-11-IDEX-0002-02 and by the Direction Générale de l’Armement, French Ministry of Defence.

The authors are with the University of Toulouse, IRIT/INP-ENSEEIHT, 31071 Toulouse, France. (e-mail: {pierreantoine.thouvenin, Nicolas.Dobigeon, Jean-Yves.Tourneret}@enseeih.fr)

works consider temporal variability by exploiting the possibilities offered by multitemporal HS (MHS) images.

From a hyperspectral unmixing perspective, MHS images, i.e., sequences of HS images acquired over the same area at different time instants, can be of interest to exploit information redundancy between consecutive images (e.g., through features exhibiting moderate or smooth temporal variations as in [11], [12]) while allowing the endmember temporal evolution to be characterized. For instance, such images have been recently exploited to improve endmember unmixing results [13]–[15] and used in a change detection problem involving two HS images [16], [17].

Even though the approaches proposed in [13]–[15] specifically allow smooth temporal variations of some of the mixture parameters to be considered, they do not account for abrupt spectral changes either due to outliers or to possibly significant time intervals between two consecutive images. In practice, such situations can be reasonably expected, depending on the acquisition dates and possible climatic hazards, e.g., when vegetation or water is present in the observed scene. Consequently, inspired by and extending the contributions in [14], [18], [19], we propose to jointly account for smooth endmember variations – construed as temporal endmember variability – and abrupt changes interpreted as outliers (e.g., significant variability within a single image or presence of nonlinearities). In particular, we specifically focus our analysis on scenes in which mostly the same materials are expected to be observed from an image to another. In this case, the endmembers identified on each single image can *in fine* be considered as time-varying instances of reference signatures shared by the different images, which justifies the use of a modified version of the perturbed linear mixing model (PLMM) proposed in [15]. The resulting unmixing problem is developed in a Bayesian framework, and inference is conducted by a Markov Chain Monte-Carlo (MCMC) method to assess the flexibility of the proposed approach.

The paper is organized as follows. The mixing model considered in this paper is introduced in Section II, and the associated Bayesian hierarchical model is developed in Section III. Section IV investigates a Gibbs sampler to solve the resulting mixed integer non-linear problem. The performance of the proposed approach on synthetic and real data is studied in Sections V and VI. In particular, the results obtained with the proposed method are compared to those of the VCA/FCLS algorithm [20], [21], the SISAL/FCLS algorithm [22], the algorithm associated with the robust LMM (rLMM) proposed in [23] and the optimization method [15]. Finally, Section VII

TABLE I
NOTATIONS.

T	number of images
N	number of pixels within each image
L	number of spectral bands
R	number of endmembers
$\mathbf{Y} \in \mathbb{R}^{L \times N \times T}$	multitemporal hyperspectral image
$\mathbf{Y}_t \in \mathbb{R}^{L \times N}$	lexicographically ordered pixels of the t th image
$\mathbf{y}_{nt} \in \mathbb{R}^L$	n th pixel of the t th image
$\mathbf{M} \in \mathbb{R}^{L \times R}$	endmember matrix
$\mathbf{dM} \in \mathbb{R}^{L \times R \times T}$	variability tensor
$\mathbf{A} \in \mathbb{R}^{R \times N \times T}$	abundance tensor
$\mathbf{X} \in \mathbb{R}^{L \times N \times T}$	outlier tensor
$\mathbf{Z} \in \mathbb{R}^{N \times T}$	binary label maps
$\beta \in \mathbb{R}^T$	granularity parameters
$\mathbf{U} \in \mathbb{R}^{A \times B \times C}$	generic three-way tensor
$\mathbf{U}_c \in \mathbb{R}^{A \times B}$	cth matrix of \mathbf{U}
$\mathbf{u}_{b,c} \in \mathbb{R}^A$	b th column of \mathbf{U}_c
$\tilde{\mathbf{u}}_{a,c} \in \mathbb{R}^{1 \times B}$	a th row of \mathbf{U}_b
\succeq	component-wise inequality
\mathcal{S}_R	unit simplex of \mathbb{R}^R
$\langle \mathbf{X}, \mathbf{Y} \rangle$	matrix inner product $\text{Tr}(\mathbf{X}^T \mathbf{Y})$
$\ \cdot\ _F$	Frobenius norm
$[\mathcal{P}]$	Inversion bracket (for a logical expression \mathcal{P} , $[\mathcal{P}] = 1$ if \mathcal{P} is true, 0 otherwise)
$\delta(x)$	$= [x = 0]$ (Kronecker symbol)
$\mathbb{1}_{\mathcal{S}}(x)$	$= [x \in \mathcal{S}]$ (indicator function)
$\sharp \mathcal{S}$	cardinal of the set \mathcal{S}
$U_{\mathcal{S}}$	uniform distribution on the set \mathcal{S}
$\mathcal{N}_{\mathcal{S}}(\boldsymbol{\mu}, \boldsymbol{\Lambda})$	multivariate Gaussian distribution, of mean $\boldsymbol{\mu}$ and covariance matrix $\boldsymbol{\Lambda}$, truncated to the set \mathcal{S}
$\bigotimes_{r=1}^R [a_r, b_r]$	$\triangleq [a_1, b_1] \times \dots \times [a_R, b_R]$.

concludes this work and outlines further research perspectives.

II. PROBLEM STATEMENT

We consider a sequence of HS images acquired at T different time instants over the same area, where mostly the same materials are expected to be observed over time. In the following, at most R endmembers are assumed to be shared between the T images composing the sequence, where R is *a priori* known. Since the observed instances of a given endmember can be reasonably expected to vary from an image to another, we propose to account for smooth endmember spectral variations via a modified version of the perturbed linear mixing model (PLMM) proposed in [7], [15]. Inspired by the total least squares problem [24], the PLMM consists in representing each pixel \mathbf{y}_{nt} by a linear combination of the R endmembers – denoted by \mathbf{m}_r – affected by an additive error term $\mathbf{dm}_{r,t}$ accounting for temporal endmember variability. In this work, an additional term $\mathbf{x}_{n,t}$ accounts for outlier contributions, i.e., significant spatial variability or nonlinearities within each image, as in [18], [23]. The resulting model can thus be written

$$\mathbf{y}_{n,t} = \sum_{r=1}^R a_{r,n,t} (\mathbf{m}_r + \mathbf{dm}_{r,t}) + \mathbf{x}_{n,t} + \mathbf{b}_{n,t} \quad (1)$$

for $n = 1, \dots, N$ and $t = 1, \dots, T$, where $\mathbf{y}_{n,t}$ denotes the n th image pixel at time t , \mathbf{m}_r is the r th endmember, $a_{r,n,t}$ is the proportion of the r th endmember in the n th pixel at time t , $\mathbf{dm}_{r,t}$ denotes the perturbation of the r th endmember at time t , and $\mathbf{x}_{n,t}$ denotes the contribution of outliers in the n th pixel at time t . Finally, $\mathbf{b}_{n,t}$ represents an additive noise resulting from the data acquisition and the modeling errors.

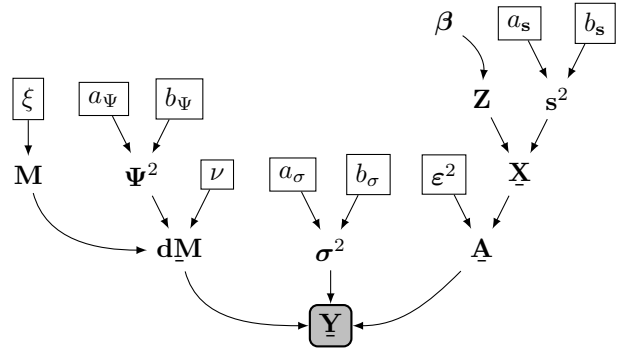


Fig. 1. Directed acyclic graph associated with the proposed Bayesian hierarchical model (fixed parameters appear in boxes).

The so-called robust PLMM (1) can be written in matrix form as

$$\mathbf{Y}_t = (\mathbf{M} + \mathbf{dM}_t) \mathbf{A}_t + \mathbf{X}_t + \mathbf{B}_t \quad (2)$$

where $\mathbf{Y}_t = [\mathbf{y}_{1,t}, \dots, \mathbf{y}_{N,t}]$ is an $L \times N$ matrix containing the pixels of the t th image, \mathbf{M} denotes an $L \times R$ matrix containing the endmembers, \mathbf{A}_t is an $R \times N$ matrix composed of the abundance vectors $\mathbf{a}_{n,t}$, \mathbf{dM}_t is an $L \times R$ matrix whose columns contain the variability inherent to the t th image, \mathbf{X}_t is an $L \times N$ matrix whose columns are the outliers present in the image t , and \mathbf{B}_t is an $L \times N$ matrix accounting for the noise at time t (see also notations in Table I). The constraints considered to reflect physical considerations are

$$\begin{aligned} \mathbf{A}_t &\succeq \mathbf{0}_{R,N}, \quad \mathbf{A}_t^T \mathbf{1}_R = \mathbf{1}_N, \quad \forall t \in \{1, \dots, T\} \\ \mathbf{M} &\succeq \mathbf{0}_{L,R}, \quad \mathbf{M} + \mathbf{dM}_t \succeq \mathbf{0}_{L,R}, \quad \forall t \in \{1, \dots, T\} \\ \mathbf{X}_t &\succeq \mathbf{0}_{L,N}, \quad \forall t \in \{1, \dots, T\} \end{aligned} \quad (3)$$

where \succeq denotes a term-wise inequality. Note that the usual abundance sum-to-one constraint will be relaxed in the following section ($\mathbf{a}_{n,t}^T \mathbf{1}_R \leq 1$) depending on the absence or presence of outliers in the pixel (n, t) . Indeed, the proposed model is intended to handle cases in which the linear model may not exhaustively describe the collected data, thus justifying the proposed relaxation. In the next section, this problem is tackled in a Bayesian framework to easily incorporate all the prior knowledge available on the mixture parameters.

III. BAYESIAN MODEL

This section details the specific structure imposed on the parameters to be inferred *via* appropriate prior distributions. Note that dependencies with respect to constant parameters are omitted in the following paragraphs to simplify the notations.

A. Likelihood

Assuming the additive noise $\mathbf{b}_{n,t}$ is distributed according to a Gaussian distribution $\mathbf{b}_{n,t} \sim \mathcal{N}(\mathbf{0}_L, \sigma_t^2 \mathbf{I}_L)$, the observation model (1) leads to

$$\mathbf{y}_{n,t} \mid \mathbf{M}, \mathbf{dM}_t, \mathbf{A}_t, \mathbf{X}_t, \sigma_t^2 \sim \mathcal{N}((\mathbf{M} + \mathbf{dM}_t) \mathbf{a}_{n,t} + \mathbf{x}_{n,t}, \sigma_t^2 \mathbf{I}_L). \quad (4)$$

In addition, assuming prior independence between the pixels within each image and between the images \mathbf{Y}_t themselves,

the likelihood function of the whole set $\mathbf{Y} = [\mathbf{Y}_1, \dots, \mathbf{Y}_T]$ of observed pixels is

$$p(\mathbf{Y} | \Theta) \propto \prod_{t=1}^T (\sigma_t^2)^{-NL/2} \times \exp\left(-\frac{1}{2\sigma_t^2} \|\mathbf{Y}_t - (\mathbf{M} + \mathbf{dM}_t)\mathbf{A}_t - \mathbf{X}_t\|_F^2\right) \quad (5)$$

where $\Theta = \{\Theta_p, \Theta_h\}$ and

$$\Theta_p = \{\mathbf{M}, \mathbf{dM}, \mathbf{A}, \mathbf{X}, \sigma^2, \mathbf{Z}\}, \Theta_h = \{\Psi^2, s^2, \beta\} \quad (6)$$

denote the parameters and hyperparameters whose priors are defined in the following paragraphs.

B. Parameter priors

1) *Outliers \mathbf{X} and label maps \mathbf{Z}* : Similarly to [18], outliers are a priori assumed to be spatially sparse. In this work however, the outliers $\mathbf{x}_{n,t}$ are assigned the following mixture prior

$$p(\mathbf{x}_{n,t} | z_{n,t}, s_t^2) = (1 - z_{n,t})\delta(\mathbf{x}_{n,t}) + z_{n,t} \mathcal{N}_{\mathbb{R}_+^L}(\mathbf{0}_L, s_t^2). \quad (7)$$

where $z_{n,t} = 1$ if an outlier is present in the corresponding pixel, and 0 otherwise. When the binary variable $z_{n,t}$ is assigned a Bernoulli prior distribution, the prior (7) results in a Bernoulli-Gaussian distribution, which has been extensively used in the literature to enforce sparsity [25], [26]. To promote spatial correlations between the outliers, the binary label maps $\mathbf{z}_t \in \mathbb{R}^N$ ($t = 1, \dots, T$) are modeled as Ising-Markov random fields [10], [27], [28], for which the Hammersley-Clifford theorem yields

$$p(\mathbf{z}_t | \beta_t) = \frac{1}{C(\beta_t)} \exp\left(\beta_t \sum_{n=1}^N \sum_{k \in \mathcal{V}(n)} \delta(z_{n,t} - z_{k,t})\right) \quad (8)$$

where $\mathcal{V}(n)$ denotes the 4-neighbourhood of the pixel n . Under appropriate independence assumptions on the label maps \mathbf{z}_t and the outliers $\mathbf{x}_{n,t}$, we obtain

$$p(\mathbf{X} | \mathbf{Z}, s^2) = \prod_{n,t} p(\mathbf{x}_{n,t} | z_{n,t}, s_t^2) \quad (9)$$

$$p(\mathbf{Z} | \beta) = \prod_{t=1}^T p(\mathbf{z}_t | \beta_t) \quad (10)$$

with $\mathbf{Z} \in \mathbb{R}^{N \times T}$ and $\beta \in \mathbb{R}^T$. Note that the prior (7) leads to the following result, which will be useful to sample the label maps in Section IV-E

$$\begin{aligned} p(\mathbf{x}_{n,t} | \mathbf{Z}_{\setminus\{z_{n,t}\}}, s_t^2, \beta_t) &= \\ &\sum_{i=0}^1 p(\mathbf{x}_{n,t} | z_{n,t} = i, \mathbf{Z}_{\setminus\{z_{n,t}\}}) \mathbb{P}[z_{n,t} = i] \\ &= (1 - \omega_{n,t})\delta(\mathbf{x}_{n,t}) + \omega_{n,t} \mathcal{N}_{\mathbb{R}_+^L}(\mathbf{0}_L, s_t^2 \mathbf{I}_L) \end{aligned}$$

with

$$\omega_{n,t} = \frac{1}{\#\mathcal{V}(n)} \exp\left(\beta_t \sum_{n=1}^N \sum_{k \in \mathcal{V}(n)} \delta(1 - z_{k,t})\right). \quad (11)$$

2) *Abundances*: We propose to promote smooth temporal variations of the abundances between successive time instants as the corresponding pixel is not classified as an outlier. This leads us to consider the following expressions, for $n = 1, \dots, N$,

$$\mathbf{a}_{n,1} | \mathbf{x}_{n,t} = \mathbf{0}_L \sim \mathcal{U}_{\mathcal{S}_R} \quad (12)$$

$$\mathbf{a}_{n,t} | \mathbf{x}_{n,t} \neq \mathbf{0}_R \sim \mathcal{U}_{\widetilde{\mathcal{S}_R}}, \text{ for } t = 1, \dots, T \quad (13)$$

$$\begin{aligned} p(\mathbf{a}_{n,t} | \mathbf{x}_{n,t} = \mathbf{0}_R, \mathbf{A}_{\setminus\{\mathbf{a}_{n,t}\}}) &\propto \\ &\exp\left\{-\frac{1}{2\varepsilon_n^2} \left([\mathcal{T}_{n,t}^1 \neq \emptyset] \|a_{n,t} - a_{n,\tau_{n,t}^1}\|_2^2 + [\mathcal{T}_{n,t}^2 \neq \emptyset] \right. \right. \\ &\left. \left. \times \|a_{n,t} - a_{n,\tau_{n,t}^2}\|_2^2 \right) \right\} \mathbb{1}_{\mathcal{S}_R}(\mathbf{a}_{n,t}), \text{ for } t = 2, \dots, T \end{aligned} \quad (14)$$

where $[\mathcal{P}]$ denotes the Inverson bracket applied to the logical proposition \mathcal{P} , i.e.,

$$[\mathcal{P}] = \begin{cases} 1, & \text{if } \mathcal{P} \text{ is true;} \\ 0, & \text{otherwise.} \end{cases}$$

and

$$\mathcal{S}_R = \{\mathbf{x} \in \mathbb{R}^R \mid \forall i, x_i \geq 0 \text{ and } \mathbf{x}^T \mathbf{1}_R = 1\} \quad (15)$$

$$\widetilde{\mathcal{S}_R} = \{\mathbf{x} \in \mathbb{R}^R \mid \forall i, x_i \geq 0 \text{ and } \mathbf{x}^T \mathbf{1}_R \leq 1\} \quad (16)$$

$$\mathcal{T}_{n,t}^1 = \{\tau < t \mid z_{n,\tau} = 0\}, \quad \tau_{n,t}^1 = \max_{\tau \in \mathcal{T}_{n,t}^1} \tau \quad (17)$$

$$\mathcal{T}_{n,t}^2 = \{\tau > t \mid z_{n,\tau} = 0\}, \quad \tau_{n,t}^2 = \min_{\tau \in \mathcal{T}_{n,t}^2} \tau. \quad (18)$$

Note that $\mathcal{T}_{n,t}^1 = \emptyset$ (resp. $\mathcal{T}_{n,t}^2 = \emptyset$) if $t = 1$ (resp. $t = T$), and that $\tau_{n,t}^1$ (resp. $\tau_{n,t}^2$) is the largest (resp. smallest) time instant before (resp. after) t associated with a pixel without outlier. Informally speaking, the above prior promotes smooth variations of the abundances associated with outlier-free pixels. In practice, for an image at time t and a pixel within this image such that $z_{n,t} = 0$, smooth variations of $\mathbf{a}_{n,t}$ are promoted *via* a one-dimensional Gaussian Markov field as in [10], [29] penalizing the Euclidean distance between $\mathbf{a}_{n,t}$ and the abundance of the last (resp. the first) corresponding outlier-free pixel in the preceding (resp. following) images of the sequence. In the following, the joint abundance prior is denoted by

$$\begin{aligned} p(\mathbf{A} | \mathbf{X}) &= \prod_{n=1}^N p(\mathbf{a}_{n,1}) \left[\prod_{j=1}^{J_n} \prod_{t_j: \mathbf{x}_{n,t_j} \neq \mathbf{0}_L} p(\mathbf{a}_{n,t_j}) \right] \\ &\times \left[\prod_{i=1}^{I_n} \prod_{t_i: \mathbf{x}_{n,t_i} = \mathbf{0}_L} p(\mathbf{a}_{n,t_i} | \mathbf{a}_{n,t_{i-1}}) \right] \end{aligned} \quad (19)$$

with $I_n = \#\{t : \mathbf{x}_{n,t} = \mathbf{0}_L\}$ and $J_n = T - I_n$.

3) *Endmembers*: A non-informative prior is adopted for the endmember matrix \mathbf{M} to reflect the absence of specific prior knowledge about the spectral signatures contained in the image. As in [18], we consider the following truncated multivariate Gaussian distribution

$$\mathbf{m}_r \sim \mathcal{N}_{\mathbb{R}_+^L}(\mathbf{0}_L, \xi \mathbf{I}_L), \text{ for } r = 1, \dots, R \quad (20)$$

where ξ is set to a sufficiently large value to ensure an uninformative prior (e.g., $\xi = 1$). Assuming the endmembers \mathbf{m}_r are independent, the joint prior for the endmembers can be written as

$$p(\mathbf{M}) = \prod_{r=1}^R p(\mathbf{m}_r). \quad (21)$$

In addition, the endmembers can be *a priori* assumed to live in a subspace of dimension $R - 1$ [30] whose practical determination can be performed by a principal component analysis (PCA) or a robust PCA (rPCA) [31]. The PCA applied to the original data \mathbf{Y} leads to [30]

$$\mathbf{m}_r = \mathbf{U}\mathbf{e}_r + \bar{\mathbf{y}}, \quad \mathbf{U}^T\mathbf{U} = \mathbf{I}_{R-1} \quad (22)$$

where \mathbf{U} denotes the projection matrix on the subspace of dimension $R - 1$ and $\bar{\mathbf{y}}$ denotes the average spectral signature obtained from \mathbf{Y} . Note that using an rPCA would result in similar expressions (modulo a simple change of notations). The prior associated with the projected endmember spectrum \mathbf{e}_r becomes

$$\mathbf{e}_r \sim \mathcal{N}_{\mathcal{E}_r}(-\mathbf{U}^T\bar{\mathbf{y}}, \xi\mathbf{I}_{R-1}), \text{ for } r = 1, \dots, R \quad (23)$$

with

$$\mathcal{E}_r = \bigotimes_{k=1}^{R-1} [e_{k,r}^-, e_{k,r}^+] \quad (24)$$

$$e_{k,r}^- = \max_{\ell \in \mathcal{U}_k^+} \left(-\frac{\bar{y}_\ell + \sum_{j \neq k} u_{\ell,j} e_{j,r}}{u_{\ell,k}} \right) \quad (25)$$

$$e_{k,r}^+ = \min_{\ell \in \mathcal{U}_k^-} \left(-\frac{\bar{y}_\ell + \sum_{j \neq k} u_{\ell,j} e_{j,r}}{u_{\ell,k}} \right) \quad (26)$$

$$\mathcal{U}_k^- = \{r : u_{k,r} < 0\}, \quad \mathcal{U}_k^+ = \{r : u_{k,r} > 0\}. \quad (27)$$

4) *Endmember variability*: We propose to consider a variability prior promoting smooth temporal variations while accounting for the term-wise positivity of the observed endmembers (i.e., $\mathbf{M} + d\mathbf{M}_t \succeq \mathbf{0}_{L,R}$), expressed as

$$\begin{aligned} d\mathbf{m}_{r,1} \mid \mathbf{m}_r &\sim \mathcal{N}_{\mathcal{I}_r}(\mathbf{0}_L, \nu \mathbf{I}_L) \\ dm_{\ell,r,t} \mid m_{\ell,r}, dm_{\ell,r,(t-1)}, \psi_{\ell,r}^2 &\sim \mathcal{N}_{\mathcal{I}_{\ell,r}}(dm_{\ell,r,(t-1)}, \psi_{\ell,r}^2) \end{aligned}$$

for $\ell = 1, \dots, L$, $r = 1, \dots, R$, $t = 1, \dots, T$, where $\mathcal{I}_r = \bigotimes_{\ell=1}^L \mathcal{I}_{\ell,r}$ and $\mathcal{I}_{\ell,r} = [-m_{\ell,r}, +\infty)$. Assuming independence between the different endmember variabilities, the joint variability prior can finally be expressed as

$$\begin{aligned} p(d\mathbf{M} \mid \mathbf{M}, \Psi^2) &= \prod_{r=1}^R \left[p(d\mathbf{m}_{r,1} \mid \mathbf{m}_r) \right. \\ &\quad \times \left. \prod_{t=2}^T p(d\mathbf{m}_{r,t} \mid \mathbf{m}_r, d\mathbf{m}_{r,(t-1)}, \psi_r^2) \right]. \end{aligned} \quad (28)$$

5) *Noise variance*: A non-informative inverse-gamma conjugate prior is selected for the noise variance

$$\sigma_t^2 \sim \mathcal{IG}(a_\sigma, b_\sigma) \quad (29)$$

for $t = 1, \dots, T$, with $a_\sigma = b_\sigma = 10^{-3}$ chosen to ensure a weakly informative prior. Assuming the noise variances are independent finally leads to

$$p(\sigma^2) = \prod_t p(\sigma_t^2). \quad (30)$$

C. Hyperparameters

In order to complete the description of the proposed hierarchical Bayesian model, we consider the following generic priors for the different hyperparameters:

- (i) non-informative conjugate inverse-gamma priors have been selected for the variability variances Ψ^2 and the outlier variances \mathbf{s}^2 , i.e., for $\ell = 1, \dots, L$, $r = 1, \dots, R$ and $t = 1, \dots, T$

$$\psi_{\ell,r}^2 \sim \mathcal{IG}(a_\Psi, b_\Psi), \quad s_t^2 \sim \mathcal{IG}(a_s, b_s) \quad (31)$$

with $a_\Psi = b_\Psi = a_s = b_s = 10^{-3}$. Classical independence assumptions for the different hyperparameters lead to

$$p(\Psi^2) = \prod_{\ell,r} p(\psi_{\ell,r}^2), \quad p(\mathbf{s}^2) = \prod_t p(s_t^2); \quad (32)$$

- (ii) the granularity parameter of a Potts-Markov random field (*a fortiori* of an Ising-Markov random field) can be reasonably restricted to the interval $[0, 2]$ [32], thus justifying the following choice¹

$$\beta_t \sim \mathcal{U}_{[0,2]}, \text{ for } t = 1, \dots, T. \quad (33)$$

Assuming the granularity parameters are independent for different time instants leads to

$$p(\beta) = \prod_t p(\beta_t). \quad (34)$$

D. Joint posterior distribution

Applying Bayes' theorem, the joint posterior distribution of the parameters of interest is given by

$$\begin{aligned} p(\Theta \mid \mathbf{Y}) &\propto p(\mathbf{Y} \mid \Theta) p(\mathbf{A} \mid \mathbf{X}) p(\mathbf{X} \mid \mathbf{Z}, \mathbf{s}^2) p(\mathbf{s}^2) \\ &\quad \times p(\mathbf{Z} \mid \beta) p(\beta) p(d\mathbf{M} \mid \mathbf{M}, \Psi^2) p(\mathbf{M}) p(\Psi^2) p(\sigma^2). \end{aligned} \quad (35)$$

The complexity of the proposed Bayesian model summarized in the directed acyclic graph of Fig. 1 and its resulting posterior (35) prevent a simple computation of the maximum *a posteriori* (MAP) or minimum mean square (MSE) estimators. Note in particular that the proposed model is parameterized by mixed continuous and integer parameters. An MCMC method is consequently adopted to sample the posterior (35) and to build estimators of the parameters involved in the proposed Bayesian model using the generated samples.

¹Greater values of the granularity parameter can be shown to almost surely lead to uniform label maps.

IV. GIBBS SAMPLER

In this section, parameter estimation is performed by using samples generated by a Gibbs sampler, which is guaranteed to produce samples asymptotically distributed according to the target distribution (35). The Gibbs sampler described in Algo. 1 consists in generating samples distributed according to the conditional distribution of each parameter of interest. To this end, the principle of Monte-Carlo methods is briefly recalled in Section IV-A, and the conditional distribution of all the parameters of interest (see Fig. 1) are detailed in the following paragraphs.

A. Bayesian inference and parameter estimation

The main steps of the proposed Gibbs sampler are summarized in Algo. 1. Similarly to [18], the sequence $\{\Theta^{(q)}\}_{q=N_{\text{bi}}+1}^{N_{\text{MC}}}$ generated by the proposed sampler (i.e., after N_{bi} burn-in iterations) is used to approximate the MMSE estimators

$$\mathbf{M}^{\text{MMSE}} = \mathbb{E} [\mathbf{M} \mid \mathbf{Y}, \Theta_{\setminus\{\mathbf{M}\}}] \quad (36)$$

$$\begin{aligned} (\mathbf{A}_t^{\text{MMSE}}, \mathbf{dM}_t^{\text{MMSE}}, \mathbf{X}_t^{\text{MMSE}}) = \\ \mathbb{E} [\mathbf{A}_t, \mathbf{dM}_t, \mathbf{X}_t \mid \mathbf{Y}_t, \Theta_{\setminus\{\mathbf{A}_t, \mathbf{dM}_t, \mathbf{X}_t\}}] \end{aligned} \quad (37)$$

where the expectations are replaced by empirical averages. Finally, the following *marginal maximum a posterior* (mMAP) estimator is considered for the label maps

$$z_{n,t}^{\text{mMAP}} = \arg \max_{z_{n,t} \in \{0,1\}} p(z_{n,t} \mid \mathbf{y}_{n,t}, \Theta_{\setminus\{z_{n,t}\}}). \quad (38)$$

More precisely, these estimators can be approximated by Monte-Carlo integration as

$$\mathbf{M}^{\text{MMSE}} \simeq \frac{1}{N_{\text{MC}} - N_{\text{bi}}} \sum_{q=N_{\text{bi}}+1}^{N_{\text{MC}}} \mathbf{M}^{(q)} \quad (39)$$

$$\mathbf{A}_t^{\text{MMSE}} \simeq \frac{1}{N_{\text{MC}} - N_{\text{bi}}} \sum_{q=N_{\text{bi}}+1}^{N_{\text{MC}}} \mathbf{A}_t^{(q)} \quad (40)$$

$$\mathbf{dM}_t^{\text{MMSE}} \simeq \frac{1}{N_{\text{MC}} - N_{\text{bi}}} \sum_{q=N_{\text{bi}}+1}^{N_{\text{MC}}} \mathbf{dM}_t^{(q)} \quad (41)$$

$$\mathbf{X}_t^{\text{MMSE}} \simeq \frac{1}{N_{\text{MC}} - N_{\text{bi}}} \sum_{q=N_{\text{bi}}+1}^{N_{\text{MC}}} \mathbf{X}_t^{(q)} \quad (42)$$

$$z_{n,t}^{\text{mMAP}} \simeq \begin{cases} 0, & \text{if } \#\{q > N_{\text{bi}} : z_{n,t}^{(q)} = 0\} \leq \frac{N_{\text{MC}} - N_{\text{bi}}}{2} \\ 1, & \text{otherwise.} \end{cases} \quad (43)$$

B. Sampling the abundances \mathbf{A}

The likelihood function (4) combined with the prior given in Section III-B2 leads to the following conditional distribution for the abundances

Algorithm 1: Proposed Gibbs sampler.

Data: $N_{\text{bi}}, N_{\text{MC}}, \mathbf{M}^{(0)}, \mathbf{A}^{(0)}, \mathbf{dM}^{(0)}, \mathbf{X}^{(0)}, \boldsymbol{\sigma}^{2(0)}, \mathbf{Z}^{(0)}, \boldsymbol{\beta}^{(0)}, \mathbf{s}^{2(0)}, \boldsymbol{\Psi}^{2(0)}$.

begin

for $q = 1$ **to** N_{MC} **do**

Sample the endmembers $\mathbf{M}^{(q)}$, cf. §IV-C ;

Sample the variability terms $\mathbf{dM}^{(q)}$, cf. §IV-D ;

Sample the abundances $\mathbf{A}^{(q)}$, cf. §IV-B ;

Sample the labels and the outliers ($\mathbf{Z}^{(q)}, \mathbf{X}^{(q)}$), cf. §IV-E ;

Sample the outlier variances $\mathbf{s}^{2(q)}$, cf. §IV-F ;

Sample the noise variances $\boldsymbol{\sigma}^{2(q)}$, cf. §IV-G ;

Sample the variability variances $\boldsymbol{\Psi}^{2(q)}$, cf. §IV-H ;

Sample the granularity parameters $\boldsymbol{\beta}^{(q)}$, cf. §IV-I ;

Result: $\{\mathbf{M}^{(q)}, \mathbf{dM}^{(q)}, \mathbf{A}^{(q)}, \mathbf{Z}^{(q)}, \mathbf{X}^{(q)}, \boldsymbol{\sigma}^{2(q)}, \mathbf{Z}^{(q)}, \boldsymbol{\beta}^{(q)}, \mathbf{s}^{2(q)}, \boldsymbol{\Psi}^{2(q)}\}_{q=1}^{N_{\text{MC}}}$.

$$\mathbf{a}_{n,t} \mid \mathbf{y}_{n,t}, \Theta_{\setminus\{\mathbf{a}_{n,t}\}} \sim \mathcal{N}_{\mathcal{S}_R}(\boldsymbol{\mu}_{n,t}^{(\mathbf{A})}, \boldsymbol{\Lambda}_{n,t}) \quad (44)$$

$$\mathbf{M}_t \triangleq \mathbf{M} + \mathbf{dM}_t \quad (45)$$

$$\boldsymbol{\Lambda}_{n,t}^{-1} = \frac{1}{\sigma_t^2} \mathbf{M}_t^T \mathbf{M}_t + \frac{1}{\varepsilon_n^2} ([\mathcal{T}_{n,t}^1 \neq \emptyset] + [\mathcal{T}_{n,t}^2 \neq \emptyset]) \mathbf{I}_R \quad (46)$$

$$\begin{aligned} \boldsymbol{\mu}_{n,t}^{(\mathbf{A})} = \boldsymbol{\Lambda}_{n,t} \left[\frac{1}{\sigma_t^2} \mathbf{M}_t^T (\mathbf{y}_{n,t} - \mathbf{x}_{n,t}) \right. \\ \left. + \frac{1}{\varepsilon_n^2} ([\mathcal{T}_{n,t}^1 \neq \emptyset] \mathbf{a}_{n,\tau_{n,t}^1} + [\mathcal{T}_{n,t}^2 \neq \emptyset] \mathbf{a}_{n,\tau_{n,t}^2}) \right]. \end{aligned} \quad (47)$$

Samples distributed according to the above truncated multivariate Gaussian distributions can be generated by a Gibbs sampler described in [33, Section IV.B.] [34], by an Hamiltonian Monte-Carlo procedure [35], [36] or by the general method recently proposed in [37]. In this work, the Gibbs sampler [33, Section IV.B.] has been adopted to sample the parameters of interest.

C. Sampling the endmembers \mathbf{M}

Combining (4) and the endmember prior given in Section III-B3 leads to

$$m_{\ell,r} \mid \mathbf{Y}, \Theta_{\setminus\{m_{\ell,r}\}} \sim \mathcal{N}_{[b_{\ell,r}, +\infty)}(\mu_{\ell,r}^{(\mathbf{M})}, \kappa_{\ell,r}^2) \quad (48)$$

$$b_{\ell,r} = \max \left\{ 0, \max_t (-dm_{\ell,r,t}) \right\} \quad (49)$$

$$\begin{aligned} \mu_{\ell,r}^{(\mathbf{M})} = \kappa_{\ell,r}^2 \sum_t \frac{1}{\sigma_t^2} \left[\tilde{\mathbf{y}}_{\ell,t} - \tilde{\mathbf{x}}_{\ell,t} - \tilde{\mathbf{m}}_{\setminus r} \mathbf{A}_{\setminus r,t} - \tilde{\mathbf{dM}}_{\ell,t} \mathbf{A}_t \right] \tilde{\mathbf{a}}_{r,t}^T \\ \kappa_{\ell,r}^2 = \left[\sum_{n,t} \frac{a_{r,n,t}^2}{\sigma_t^2} + \frac{1}{\xi} \right]^{-1} \end{aligned} \quad (50)$$

$$(51)$$

where $\tilde{\mathbf{u}}_{\ell,t}$ is the ℓ th row of a given matrix \mathbf{U}_t . Samples distributed according to the above truncated Gaussian distributions can be efficiently generated using the algorithm described in [38]. When using a PCA as a preprocessing step (22), the

projected endmembers \mathbf{e}_r , for $r = 1, \dots, R$ follow a truncated multivariate Gaussian distribution [30]

$$\mathbf{e}_r \mid \mathbf{Y}, \Theta_{\setminus \{\mathbf{e}_r\}} \sim \mathcal{N}_{\mathcal{E}_r}(\boldsymbol{\mu}_r^{(\mathbf{E})}, \boldsymbol{\Lambda}_r) \quad (52)$$

where \mathcal{E}_r , $\boldsymbol{\mu}_r^{(\mathbf{E})}$ and $\boldsymbol{\Lambda}_r$ are defined in Appendix A to ease the reading of this paper.

D. Sampling the variability terms \mathbf{dM}

Similarly, the likelihood function (4) and the prior given in Section III-B4 lead to

$$dm_{\ell,r,t} \sim \mathcal{N}_{[-m_{\ell,r,t}, +\infty)}(\mu_{\ell,r,t}^{(\mathbf{dM})}, \eta_{\ell,r,t}^2) \quad (53)$$

with

$$\begin{aligned} \frac{1}{\eta_{\ell,r,t}^2} = & \frac{1}{\sigma_t^2} \sum_n a_{r,n,t}^2 + \frac{1}{\nu} [t = 1] \\ & + \frac{1}{\psi_{\ell,r}^2} (1 + [1 < t < T]) \end{aligned} \quad (54)$$

$$\begin{aligned} \mu_{\ell,r,t}^{(\mathbf{dM})} = & \left[\frac{1}{\sigma_t^2} (\tilde{\mathbf{y}}_{\ell,t} - \widetilde{\mathbf{dM}}_{\ell,\setminus r,t} \mathbf{a}_{\setminus r,t} - \tilde{\mathbf{m}}_{\ell} \mathbf{a}_{n,t} - \mathbf{x}_{\ell,n,t}) \mathbf{a}_{n,t} \right. \\ & \left. + \frac{1}{\psi_{\ell,r}^2} ([t < T] dm_{\ell,r,(t+1)} + [t > 1] dm_{\ell,r,(t-1)}) \right] \eta_{\ell,r,t}^2 \end{aligned} \quad (55)$$

where $\widetilde{\mathbf{dM}}_{\ell,\setminus r,t}$ denotes the ℓ th row of \mathbf{dM}_t deprived of its r th element, and $\tilde{\mathbf{m}}_{\ell}$ is the ℓ th row of \mathbf{M} .

E. Sampling the label maps \mathbf{Z} and the outliers \mathbf{X}

According to (4) and III-B1, the outliers admit the following group-sparsity promoting conditional distributions

$$\begin{aligned} p(\mathbf{x}_{n,t} \mid \mathbf{y}_{n,t}, \Theta_{\setminus \{z_{n,t}, \mathbf{x}_{n,t}\}}) = & \\ (1 - w_{n,t}) \delta(\mathbf{x}_{n,t}) + w_{n,t} \mathcal{N}_{\mathbb{R}_+^L}(\boldsymbol{\mu}_{n,t}, \vartheta_t^2 \mathbf{I}_L) \end{aligned} \quad (56)$$

which are mixtures of a Dirac mass at $\mathbf{0}$ and of truncated multivariate Gaussian distributions, where

$$w_{n,t} = \frac{\tilde{w}_{n,t}}{\tilde{w}_{n,t} + (1 - w_{n,t})}, \quad \vartheta_t^2 = \frac{\sigma_t^2 s_t^2}{\sigma_t^2 + s_t^2} \quad (57)$$

$$\tilde{w}_{n,t} = \frac{\omega_{n,t}}{(s_t^2)^{L/2}} (\vartheta_t^2)^{L/2} \exp\left(\frac{1}{2\vartheta_t^2} \|\boldsymbol{\mu}_{n,t}\|_2^2\right) \quad (58)$$

$$\boldsymbol{\mu}_{n,t}^{(\mathbf{X})} = \frac{s_t^2}{\sigma_t^2 + s_t^2} [\mathbf{y}_{n,t} - (\mathbf{M} + \mathbf{dM}_t) \mathbf{a}_{n,t}]. \quad (59)$$

In practice, the labels $z_{n,t}$ are first sampled to select one of the two models for $\mathbf{x}_{n,t}$, with probability $\mathbb{P}[z_{n,t} = 1 \mid \mathbf{y}_{n,t}, \Theta_{\setminus \{z_{n,t}, \mathbf{x}_{n,t}\}}] = w_{n,t}$.

F. Sampling the outlier variances \mathbf{s}^2

According to Section III-B1 and III-C, we can easily identify the conditional law of s_t^2 for $t = 1, \dots, T$ as the following inverse gamma distribution

$$s_t^2 \mid \Theta_{\setminus \{s_t^2\}} \sim \mathcal{IG}\left(a_s + \frac{\#\{n : z_{n,t} = 1\}L}{2}, b_s + \frac{1}{2} \|\mathbf{X}_t\|_F^2\right). \quad (60)$$

G. Sampling the noise variances σ^2

Using Sections III-B5 and III-C, we obtain

$$\begin{aligned} \sigma_t^2 \mid \mathbf{Y}_t, \Theta_{\setminus \{\sigma_t^2\}} \sim & \\ \mathcal{IG}\left(a_\sigma + \frac{LN}{2}, b_\sigma + \frac{1}{2} \|\mathbf{Y}_t - (\mathbf{M} + \mathbf{dM}_t) \mathbf{A}_t - \mathbf{X}_t\|_F^2\right) \end{aligned} \quad (61)$$

for $t = 1, \dots, T$.

H. Sampling the variability variances Ψ^2

Similarly, Section III-B4 and III-C lead to

$$\begin{aligned} \psi_{\ell,r}^2 \mid \Theta_{\setminus \{\psi_{\ell,r}^2\}} \sim & \\ \mathcal{IG}\left(a_\Psi + \frac{T-1}{2}, b_\Psi + \frac{1}{2} \sum_{t=2}^T (dm_{\ell,r,t} - dm_{\ell,r,t-1})^2\right). \end{aligned} \quad (62)$$

I. Sampling the granularity parameters β

Provided square images are considered, the partition functions $C(\beta_t)$ admit the following closed-form expression [39], [40]

$$\tilde{C}(\beta_t) = \log C(\beta_t)/N \quad (63)$$

$$\tilde{C}(\beta_t) = \beta_t + \frac{1}{2} \log(2 \sinh \beta_t) + \frac{1}{2N} \sum_{n=1}^N \operatorname{acosh} \Delta_n(\beta_t) \quad (64)$$

$$\Delta_n(\beta_t) = v(\beta_t) - C_n, \quad v(\beta_t) = \frac{\cosh^2 \beta_t}{\sinh \beta_t} \quad (65)$$

$$C_n = \cos\left(\frac{2n-1}{2N}\pi\right). \quad (66)$$

The exact partition function can then be used to sample the parameters β_t using Metropolis-Hastings steps. In this work, new values of the granularity parameters have been proposed by the following Gaussian random walk

$$\beta_t^* = \beta_t^{(q)} + \varepsilon_t, \quad \varepsilon_t \sim \mathcal{N}(0, \sigma_\beta^2(t)) \quad (67)$$

where the parameters $\sigma_\beta^2(t)$ are adjusted during the burn-in iterations to yield acceptance rates in the interval [0.4, 0.6]. More precisely, the acceptance rates ρ_t are given by

$$\begin{aligned} \rho_t = \max & \left(1, \frac{C(\beta_t^{(q)})}{C(\beta_t^*)} \frac{\mathbb{1}_{[0,2]}(\beta_t^*)}{\mathbb{1}_{[0,2]}(\beta_t^{(q)})} \right. \\ & \left. \times \exp\left[\frac{1}{2}(\beta_t^* - \beta_t^{(q)}) \sum_{n=1}^N \sum_{k \in \mathcal{V}(n)} \delta(z_{n,t} - z_{k,t})\right] \right). \end{aligned} \quad (68)$$

V. EXPERIMENTS WITH SYNTHETIC DATA

The proposed method has been applied to MHS images composed of 10 acquisitions of size 50×50 with $L = 413$ bands. The first scenario deals with the apparition of a new material in specific regions of a few images. To this end, 4 images out of the 10 have been corrupted by spatially sparse outliers, corresponding to a new endmember taken from a spectral

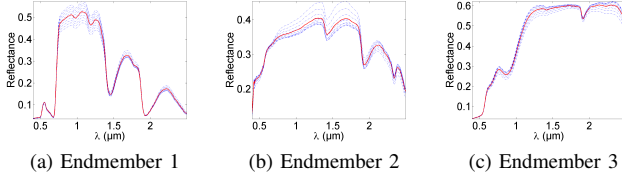


Fig. 2. Endmembers (red lines) and variability (blue dotted lines) used to generate the synthetic mixtures with $R = 3$.

TABLE II
PARAMETERS USED IN THE EXPERIMENTS.

	Synthetic data	Real data
σ_t^2	10^{-4}	10^{-4}
s_t^2	5×10^{-3}	5×10^{-3}
$\psi_{\ell,r}^2$	10^{-3}	10^{-4}
ε_n^2	10^{-3}	10^{-3}
ξ	1	1
β_t	1.9	1.7
ν	10^{-3}	10^{-5}
a_s, a_Ψ, a_σ	10^{-3}	10^{-3}
b_s, b_Ψ, b_σ	10^{-3}	10^{-3}
N_{bi}	350	450
N_{MC}	400	500

library. Each image of the sequence corresponds to a linear mixture of 3 endmembers affected by smooth time-varying variability, and the synthetic abundances vary smoothly from one image to another. Note that the temporal variations of the variability and the abundances have been generated from the parameters of the first image with trigonometric functions. The mixtures have finally been corrupted by an additive white Gaussian noise to ensure a resulting signal-to-noise ratio between 25 and 30 dB. Similarly, two complementary scenarii involving 5 HS images, of size 100×100 , composed of 6 and 9 endmembers, have been considered to analyze the performance of the method in the presence of a larger number of endmembers. Note that all the images of this experiment do not satisfy the pure pixel assumption to allow the flexibility of the proposed method to be assessed in challenging situations.

Controlled spectral variability has been introduced by using the product of reference endmembers with randomly generated piecewise-affine functions as in [7], where different affine functions have been generated for each endmember at each time instant. Typical instances of the signatures used in this experiment are depicted in Fig. 2.

A. Compared methods

The results of the proposed algorithm have been compared to those of several unmixing methods from the literature, some of which are specifically designed to unmix a single HS image. In the following lines, the most relevant implementation details specific to each method are briefly recalled.

- 1) VCA/FCLS (no variability): the endmembers are first extracted on each image using the vertex component analysis (VCA) [20], which requires pure pixels to be present. The abundances are then estimated for each pixel by solving a fully constrained least squares problem (FCLS)

TABLE III
SIMULATION RESULTS ON SYNTHETIC DATA (aSAM(M) IN ($^{\circ}$), GMSE(A) $\times 10^{-2}$, GMSE(dM) $\times 10^{-4}$, RE $\times 10^{-4}$, TIME IN (S)).

	aSAM(M)	GMSE(A)	GMSE(dM)	RE	time
$R = 3$	VCA/FCLS	6.07	2.32	/	3.91 1
	SISAL/FCLS	5.07	1.71	/	2.28 2
	rLMM	5.13	2.04	/	0.31 463
	OU	1.90	0.42	3.22	2.61 98
	Proposed	2.03	0.15	1.85	2.00 2530
$R = 6$	VCA/FCLS	3.81	1.57	/	3.09 2
	SISAL/FCLS	5.76	0.91	/	4.49 3
	rLMM	2.73	1.26	/	0.29 1453
	OU	2.74	0.38	3.70	1.13 420
	Proposed	1.48	0.16	2.84	0.51 8691
$R = 9$	VCA/FCLS	3.62	0.57	/	2.16 3
	SISAL/FCLS	7.08	0.69	/	12.1 4
	rLMM	2.45	0.53	/	0.38 1446
	OU	1.64	0.19	2.10	1.15 203
	Proposed	2.75	0.21	3.04	0.86 10408

using the Alternating Direction Method of Multipliers (ADMM) [21];

- 2) SISAL/FCLS (no variability): the endmembers are extracted on each image by the simplex identification via split augmented Lagrangian (SISAL) [22], and the abundances are estimated for each pixel by FCLS. The tolerance for the stopping rule has been set to 10^{-3} ;
- 3) OU: the endmembers are estimated using the online unmixing (OU) algorithm introduced in [15] with endmembers initialized by the output of VCA applied to the first image of the sequence. The abundances are initialized by FCLS, and the variability matrices are initialized with all their entries equal to 0. The other parameters are set to the same values as those given in [15, Table I];
- 4) rLMM (no variability): the unmixing method associated with the robust linear mixing model (rLMM) proposed in [23] has been applied to each image of the series independently. The algorithm has been initialized with VCA/FCLS, and the regularization parameter specific to this method is set as suggested in [23];
- 5) Proposed approach: the endmembers are initialized with VCA applied to the first image of the sequence. The abundances are initialized by FCLS, and the variability matrices and label maps are initialized with all their entries equal to 0 (i.e., the images are a priori assumed to contain no outlier). The values for the other parameters are summarized in Table II.

Performance assessment has been conducted in terms of

- endmember estimation through the average spectral angle mapper (aSAM)

$$aSAM(M) = \frac{1}{R} \sum_{r=1}^R \arccos \left(\frac{\mathbf{m}_r^T \hat{\mathbf{m}}_r}{\|\mathbf{m}_r\|_2 \|\hat{\mathbf{m}}_r\|_2} \right); \quad (69)$$

- abundance and variability estimation through the global mean square errors (GMSEs)

$$GMSE(A) = \frac{1}{TRN} \sum_{t=1}^T \|\mathbf{A}_t - \hat{\mathbf{A}}_t\|_F^2 \quad (70)$$

$$GMSE(dM) = \frac{1}{TLR} \sum_{t=1}^T \|\mathbf{dM}_t - \hat{\mathbf{dM}}_t\|_F^2; \quad (71)$$

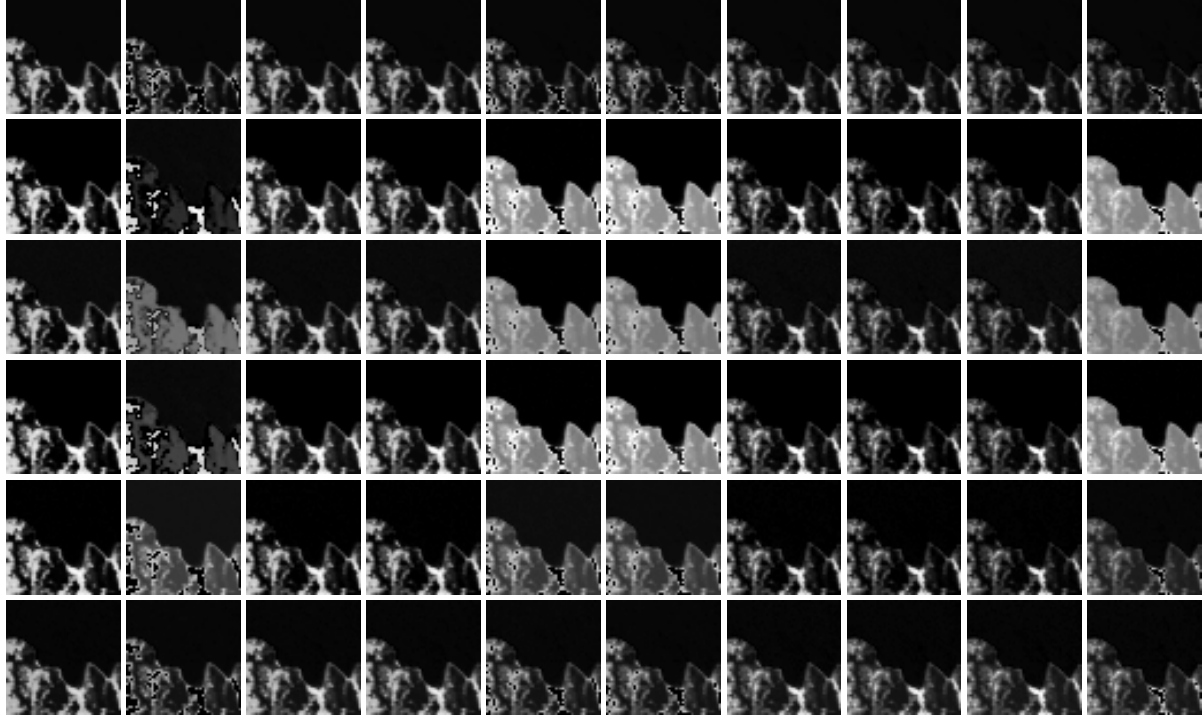


Fig. 4. Abundance map of the first endmember recovered by the different methods (in each row) at each time instant (given in column) for the experiment with $R = 3$ [true abundances on the first row, VCA/FCLS on the second row, SISAL/FCLS on the third row, rLMM on the fourth row, OU on the fifth row, proposed method on the last row]. Due to space restrictions, the abundance maps of the two other endmembers have been included in the technical report [41].

(iii) quadratic reconstruction error (RE)

$$RE = \frac{1}{TLN} \sum_{t=1}^T \|\mathbf{Y}_t - \hat{\mathbf{Y}}_t\|_F^2 \quad (72)$$

where $\hat{\mathbf{Y}}_t$ is the matrix composed of the pixels reconstructed with the estimated parameters.

B. Results

The endmembers estimated by the proposed algorithm are compared to those of VCA/FCLS, SISAL/FCLS, rLMM and OU in Fig. 3, whereas the corresponding abundance maps are displayed in Fig. 4. The abundance maps and the endmembers obtained on the mixtures with 6 and 9 endmembers are included in a separate technical report [41] due to space constraints. The unmixing performance of each method, reported in Table III, leads to the following conclusions.

- The proposed method shows a satisfactory robustness with respect to spatially sparse outliers. In comparison, the shape of the endmembers recovered by VCA, SISAL and rLMM and the variability extracted by OU are significantly affected by outliers, as exemplified in Figs. 3b, 3e, 3h and 3k respectively. Note that the endmembers recovered by the rLMM are significantly influenced by the VCA initialization. In addition, the abundance maps estimated by FCLS appear to be highly sensitive to the presence of outliers (see Figs. 4);
- The proposed algorithm presents lower or similar reconstruction/estimation errors when compared to all the other methods;

- As expected, the proposed approach based on an MCMC method is computationally more expensive;
- Even though the performance of the proposed method degrades with the number of endmembers involved in the mixtures, it proves relatively robust when compared to the other methods, especially VCA and SISAL.

In addition, as a complementary output, the proposed algorithm is able to recover the presence and location of the outliers, as illustrated in Fig. 5.

VI. EXPERIMENT WITH REAL DATA

A. Description of the dataset

The proposed approach has been applied to a real sequence of AVIRIS HS images acquired over the Lake Tahoe region (California, United States of America) between 2014 and 2015². The scene of interest (50×50), composed of a lake and a nearby field, has been unmixed with $R = 3$ endmembers based on the results of the noise-whitened eigengap algorithm (NWEGA) [42] applied to each image of the series (see Table IV). After removing the seemingly corrupted bands and the water absorption bands, 173 out of the 224 spectral bands were finally exploited.

The initial parameters used for the proposed algorithm are given in Table II, and the other methods have been run with the same parameters as in Section V.

²The images used in this experiment are freely available from the online AVIRIS flight locator tool at http://aviris.jpl.nasa.gov/alt_locator/.

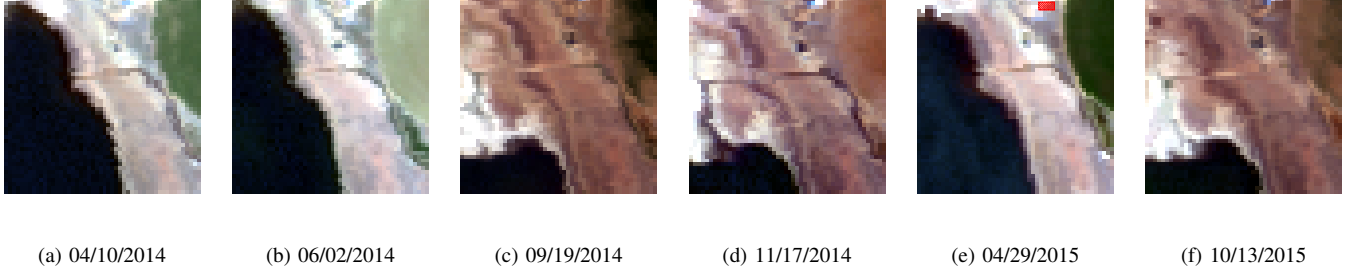


Fig. 6. Scenes used in the experiment, given with their respective acquisition date. The area delineated in red in Fig. 6e highlights a region known to contain outliers (this observation results from a previous analysis led on this dataset in [15]).

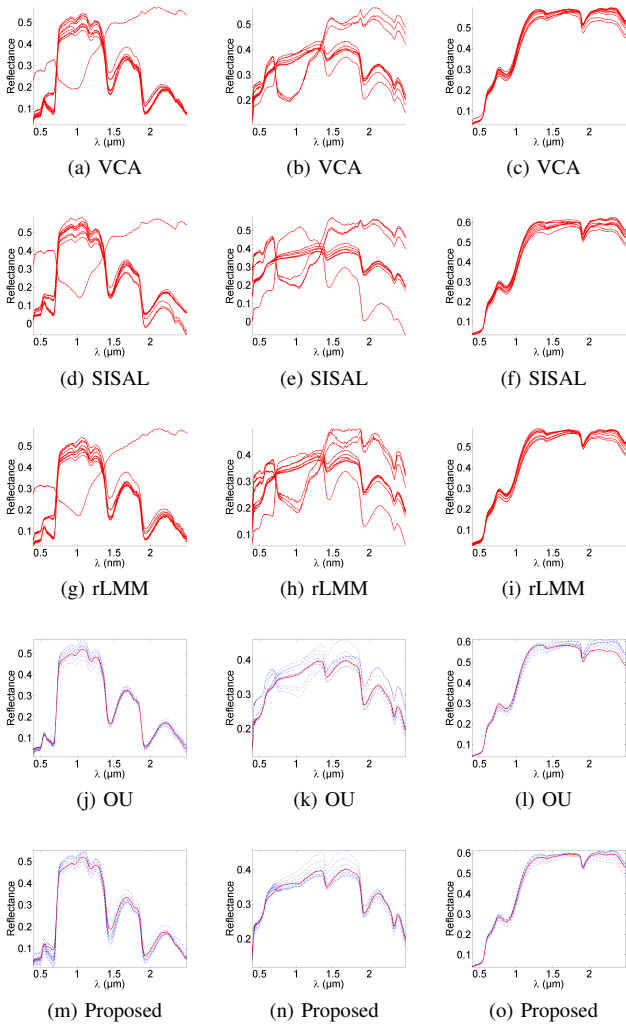


Fig. 3. Endmembers (red lines) and variability (blue dotted lines) recovered by the different methods from the synthetic mixtures with $R = 3$.

B. Results

In the absence of any ground truth, the performance of the unmixing methods is assessed in terms of RE while taking into account the consistency of the estimated abundance maps reported in Figs. 8, 9 and 10. The proposed method provides better reconstruction errors (see Table V), and yields more consistent abundance maps especially for the soil and the

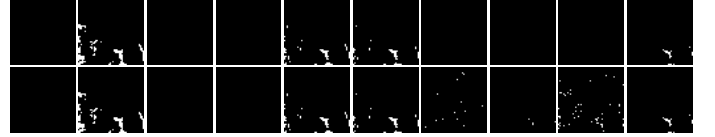


Fig. 5. Outlier labels z_t estimated for each image of the synthetic dataset with 3 endmembers (true labels on the first row, estimated labels on the second row) [0 in black, 1 in white].

TABLE IV
ENDMEMBER NUMBER R ESTIMATED BY NWEWA [42] ON EACH IMAGE OF THE REAL DATASET.

	04/10/2014	06/02/2014	09/19/2014	11/17/2014	04/29/2015	10/13/2015
NWEWA	3	3	3	4	3	4

water.

In particular, note that VCA and SISAL inevitably capture the significant outlier contribution highlighted in Fig. 6e, as exemplified by the abundance maps reported at the intersection of the fifth column and the two first rows of Figs. 8 and 9. The corresponding signatures, depicted in Figs. 7d and 7a for VCA and SISAL, have an amplitude significantly greater than 1. In particular, VCA fails to extract the faint traces of dry vegetation (see the fourth column of Fig. 10) contrary to the other methods. From this point of view, OU and the proposed method yield much more consistent abundance maps.

The results, reported in Table V and in Figs. 7, 8, 9, 10 and 11 suggest that the proposed approach is robust to spatially sparse outliers while allowing smooth temporal variations to be exploited. Indeed, the outliers previously detected in this dataset [15] (highlighted in red in Fig. 6e) are well captured by the latent variables Z . In addition, the spatial distribution of the estimated outlier labels (reported in Fig. 11) is in accordance with the results of the rLMM and with the non-linearity detector [43] applied to each image of the sequence with the SISAL-estimated endmembers (see Fig. 12). Concentrated on regions where non-linear effects can be reasonably expected, the active latent variables Z tend to capture the spatial distribution of the non-linearities possibly occurring in the observed scene.

TABLE V
SIMULATION RESULTS ON REAL DATA (RE $\times 10^{-4}$).

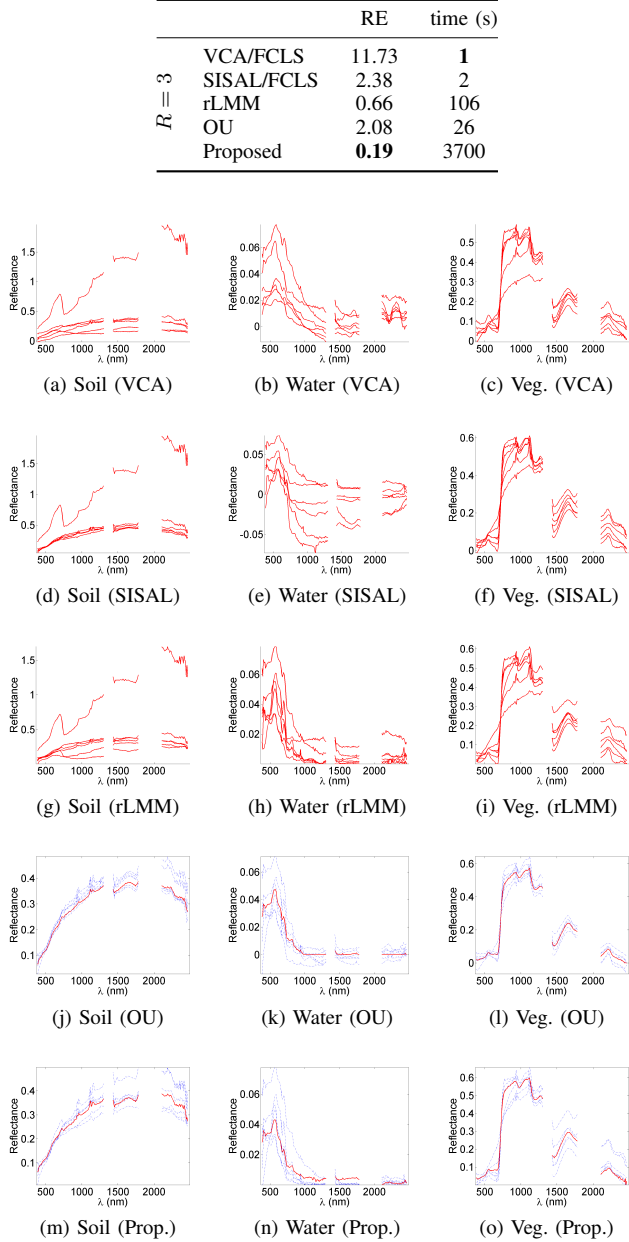


Fig. 7. Endmembers (red lines) and variability (blue dotted lines) recovered by the different methods from the real dataset depicted in Fig. 6.

VII. CONCLUSION AND FUTURE WORK

This paper introduced a Bayesian model accounting for both smooth and abrupt variations possibly occurring in multitemporal hyperspectral images. The adopted model was specifically designed to handle datasets in which mostly the same materials were expected to be observed at different time instants, thus allowing redundancy in temporal information to be exploited.

An MCMC algorithm was derived to solve the resulting unmixing problem in order to precisely assess the performance of the proposed approach on multitemporal HS images of moderate size (i.e., moderate spatial and temporal dimensions). This algorithm was used to sample the posterior of

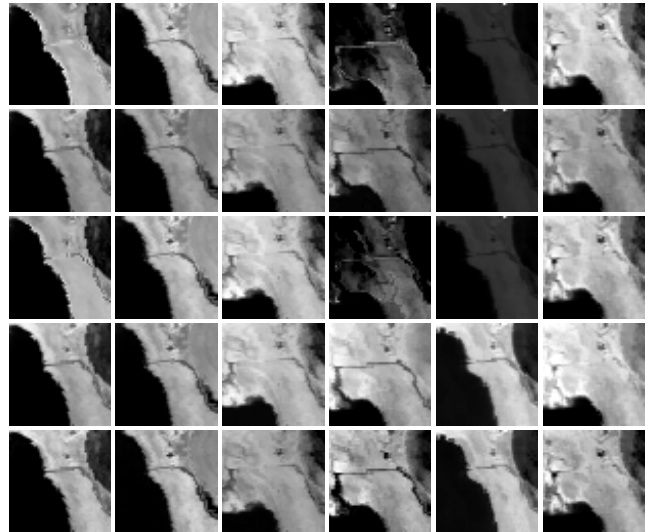


Fig. 8. Soil abundance map recovered by the different methods (in each row) at each time instant (given in column) for the experiment on the real dataset [VCA/FCLS on the first row, SISAL/FCLS on the second row, rLMM on the third row, OU on the fourth row, proposed method on the last row].

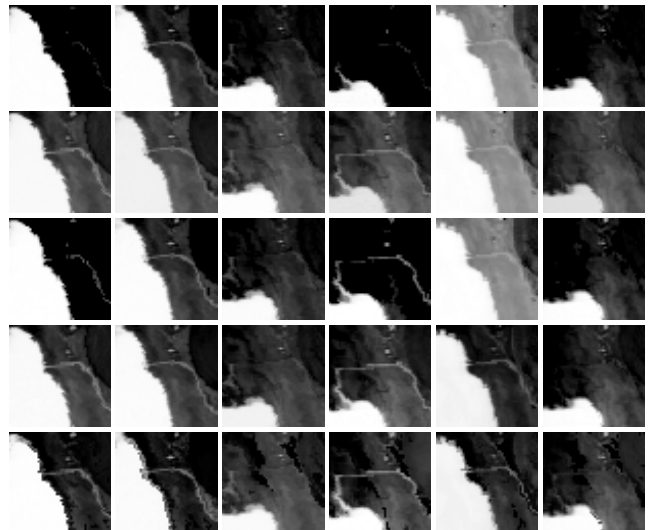


Fig. 9. Water abundance map recovered by the different methods (in each row) at each time instant (given in column) for the experiment on the real dataset [VCA/FCLS on the first row, SISAL/FCLS on the second row, rLMM on the third row, OU on the fourth row, proposed method on the last row].

the proposed hierarchical Bayesian model and to use the generated samples to build estimators of the unknown model parameters. Future research perspectives include the use of relaxation methods to the Ising field to tackle similar problems with online optimization techniques, and the development of distributed unmixing procedures to efficiently unmix larger datasets.

APPENDIX A SAMPLING THE PROJECTED ENDMEMBERS

When using a PCA as a preprocessing step, the projected endmembers \mathbf{e}_r , for $r = 1, \dots, R$, are distributed according

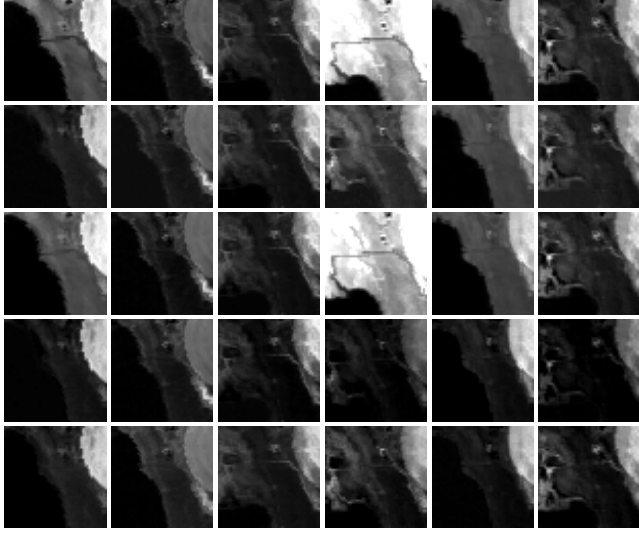


Fig. 10. Vegetation abundance map recovered by the different methods (in each row) at each time instant (given in column) for the experiment on the real dataset [VCA/FCLS on the first row, SISAL/FCLS on the second row, rLMM on the third row, OU on the fourth row, proposed method on the last row].

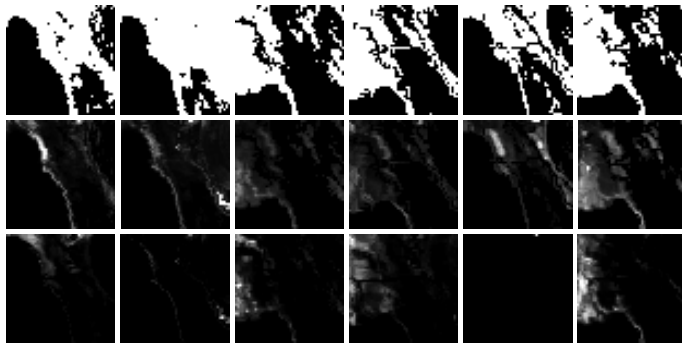


Fig. 11. mMAP estimates of the label maps recovered by the proposed approach, displayed at each time instant (label map on the first row where pixels detected as outliers appear in white, outlier energy map re-scaled in the interval $[0, 1]$ obtained by the proposed method on the second row, and by rLMM on the last row).

to the following Gaussian distributions

$$\mathbf{e}_r \mid \mathbf{Y}, \Theta_{\setminus \{\mathbf{e}_r\}} \sim \mathcal{N}_{\mathcal{E}_r}(\boldsymbol{\mu}_r^{(\mathbf{E})}, \boldsymbol{\Lambda}_r) \quad (73)$$



Fig. 12. Non-linearity maps estimated by the detector [43] applied to each image with the SISAL-extracted endmembers, with a probability of false alarm set to 10^{-3} (pixels detected as non-linearities appear in white).

with

$$\mathcal{E}_r = \bigotimes_{k=1}^{R-1} [c_{k,r}, d_{k,r}] \quad (74)$$

$$b_{\ell,r} = \min \left\{ 0, \min_t (dm_{\ell,r,t}) \right\} \quad (75)$$

$$c_{k,r} = \max_{\ell \in \mathcal{U}_k^+} \left(-\frac{\bar{y}_\ell + \sum_{j \neq k} u_{\ell,j} e_{j,r} + b_{\ell,r}}{u_{\ell,k}} \right) \quad (76)$$

$$d_{k,r} = \min_{\ell \in \mathcal{U}_k^-} \left(-\frac{\bar{y}_\ell + \sum_{j \neq k} u_{\ell,j} e_{j,r} + b_{\ell,r}}{u_{\ell,k}} \right) \quad (77)$$

$$\boldsymbol{\Lambda}_r^{-1} = \left[\sum_{n,t} \frac{a_{r,n,t}^2}{\sigma_t^2} + \frac{1}{\xi} \right] \mathbf{I}_{R-1} \quad (78)$$

$$\begin{aligned} \boldsymbol{\mu}_r^{(\mathbf{E})} = \boldsymbol{\Lambda}_r \mathbf{U}^T & \left[\sum_{t,n} \frac{1}{\sigma_t^2} \left(\mathbf{y}_{n,t} - \mathbf{x}_{n,t} - \mathbf{dM}_t \mathbf{a}_{n,t} \right. \right. \\ & \left. \left. - \bar{\mathbf{y}} a_{r,n,t} - \sum_{j \neq r} a_{j,n,t} \mathbf{m}_j \right) a_{r,n,t} - \frac{1}{\xi} \bar{\mathbf{y}} \right]. \end{aligned} \quad (79)$$

REFERENCES

- [1] J. M. Bioucas-Dias, A. Plaza, N. Dobigeon, M. Parente, Q. Du, P. Gader, and J. Chanussot, "Hyperspectral unmixing overview: Geometrical, statistical, and sparse regression-based approaches," *IEEE J. Sel. Topics Appl. Earth Observ. in Remote Sens.*, vol. 5, no. 2, pp. 354–379, April 2012.
- [2] B. Somers, G. P. Asner, L. Tits, and P. Coppin, "Endmember variability in spectral mixture analysis: A review," *Remote Sens. Environment*, vol. 115, no. 7, pp. 1603–1616, July 2011.
- [3] A. Zare and K. C. Ho, "Endmember variability in hyperspectral imagery," *IEEE Signal Process. Mag.*, vol. 31, no. 1, pp. 95–104, Jan. 2014.
- [4] B. Somers, M. Zortea, A. Plaza, and G. Asner, "Automated extraction of image-based endmember bundles for improved spectral unmixing," *IEEE J. Sel. Topics Appl. Earth Observ. in Remote Sens.*, vol. 5, no. 2, pp. 396–408, April 2012.
- [5] M. A. Veganzonés, L. Drumetz, G. Tochon, M. D. Mura, A. Plaza, J. M. Bioucas-Dias, and J. Chanussot, "A new extended linear mixing model to address spectral variability," in *Proc. IEEE GRSS Workshop Hyperspectral Image Signal Process.: Evolution in Remote Sens. (WHISPERS)*, Lausanne, Switzerland, June 2014.
- [6] T. Uezato, R. J. Murphy, A. Melkumyan, and A. Chlingaryan, "A novel spectral unmixing method incorporating spectral variability within endmember classes," *IEEE Trans. Geosci. Remote Sens.*, vol. 54, no. 5, pp. 2812–2831, March 2016.
- [7] P.-A. Thouvenin, N. Dobigeon, and J.-Y. Tourneret, "Hyperspectral unmixing with spectral variability using a perturbed linear mixing model," *IEEE Trans. Signal Process.*, vol. 64, no. 2, pp. 525–538, Jan. 2016.
- [8] O. Eches, N. Dobigeon, C. Mailhes, and J.-Y. Tourneret, "Bayesian estimation of linear mixtures using the normal compositional model. Application to hyperspectral imagery," *IEEE Trans. Image Process.*, vol. 19, no. 6, pp. 1403–1413, June 2010.
- [9] X. Du, A. Zare, P. Gader, and D. Dranishnikov, "Spatial and spectral unmixing using the beta compositional model," *IEEE J. Sel. Topics Appl. Earth Observ. in Remote Sens.*, vol. 7, no. 6, pp. 1994–2003, June 2014.
- [10] A. Halimi, N. Dobigeon, and J.-Y. Tourneret, "Unsupervised unmixing of hyperspectral images accounting for endmember variability," *IEEE Trans. Image Process.*, vol. 24, no. 12, pp. 4904–4917, Dec. 2015.
- [11] A. Halimi, C. Mailhes, and J.-Y. Tourneret, "Nonlinear regression using smooth Bayesian estimation," in *Proc. IEEE Int. Conf. Acoust., Speech, and Signal Processing (ICASSP)*, Brisbane, Australia, April 2015, pp. 2634–2638.
- [12] A. Halimi, C. Mailhes, J.-Y. Tourneret, and H. Snoussi, "Bayesian estimation of smooth altimetric parameters: Application to conventional and delay/Doppler altimetry," *IEEE Trans. Geosci. Remote Sens.*, vol. 54, no. 4, pp. 2207–2219, April 2016.

[13] S. Henrot, J. Chanussot, and C. Jutten, "Dynamical spectral unmixing of multitemporal hyperspectral images," *IEEE Trans. Image Process.*, vol. 25, no. 7, pp. 3219–3232, July 2016.

[14] A. Halimi, N. Dobigeon, J.-Y. Tourneret, S. McLaughlin, and P. Honeine, "Unmixing hyperspectral images accounting for temporal and spatial endmember variability," in *Proc. European Signal Process. Conf. (EUSIPCO)*, Nice, France, Sept. 2015, pp. 1686–1690.

[15] P.-A. Thouvenin, N. Dobigeon, and J.-Y. Tourneret, "Online unmixing of multitemporal hyperspectral images accounting for spectral variability," *IEEE Trans. Image Process.*, vol. 25, no. 9, pp. 3979–3990, Sept. 2016.

[16] A. Ertürk and A. Plaza, "Informative Change Detection by Unmixing for Hyperspectral Images," *IEEE Geosci. Remote Sens. Lett.*, vol. 12, no. 6, pp. 1252–1256, June 2015.

[17] S. Liu, L. Bruzzone, F. Bovolo, and P. Du, "Unsupervised multitemporal spectral unmixing for detecting multiple changes in hyperspectral images," *IEEE Trans. Geosci. Remote Sens.*, vol. 54, no. 5, pp. 2733–2748, May 2016.

[18] Y. Altmann, S. McLaughlin, and A. O. Hero, "Robust linear spectral unmixing using anomaly detection," *IEEE Trans. Comput. Imag.*, vol. 1, no. 2, pp. 74–85, June 2015.

[19] C. Chenot, J. Bobin, and J. Rapin, "Robust sparse blind source separation," *IEEE Signal Process. Lett.*, vol. 22, no. 11, pp. 2172–2176, Nov. 2015.

[20] J. M. Nascimento and J. M. Bioucas-Dias, "Vertex component analysis: a fast algorithm to unmix hyperspectral data," *IEEE Trans. Geosci. Remote Sens.*, vol. 43, no. 4, pp. 898–910, April 2005.

[21] J. M. Bioucas-Dias and M. A. T. Figueiredo, "Alternating direction algorithms for constrained sparse regression: Application to hyperspectral unmixing," in *Proc. IEEE GRSS Workshop Hyperspectral Image Signal Process.: Evolution in Remote Sens. (WHISPERS)*, Reykjavik, Iceland, June 2010.

[22] J. M. Bioucas-Dias, "A variable splitting augmented Lagrangian approach to linear spectral unmixing," in *Proc. IEEE GRSS Workshop Hyperspectral Image Signal Process.: Evolution in Remote Sens. (WHISPERS)*, Grenoble, France, Aug. 2009.

[23] C. Févotte and N. Dobigeon, "Nonlinear hyperspectral unmixing with robust nonnegative matrix factorization," *IEEE Trans. Image Process.*, vol. 24, no. 12, pp. 4904–4917, Dec. 2015.

[24] G. H. Golub and C. F. V. Loan, "An analysis of the total least squares problem," *SIAM J. Numer. Anal.*, vol. 17, no. 6, pp. 883 – 893, Dec. 1980.

[25] C. Bazot, N. Dobigeon, and J.-Y. Tourneret, "Bernoulli-Gaussian model for gene expression analysis," in *Proc. IEEE Int. Conf. Acoust., Speech, and Signal Processing (ICASSP)*, Prague, Czech Republic, May 2011, pp. 5996–5999.

[26] L. Chaari, J.-Y. Tourneret, and C. Chaux, "Sparse signal recovery using a Bernoulli generalized Gaussian prior," in *Proc. European Signal Process. Conf. (EUSIPCO)*, Nice, France, Sept. 2015, pp. 1711–1715.

[27] O. Eches, N. Dobigeon, and J. Y. Tourneret, "Enhancing hyperspectral image unmixing with spatial correlations," *IEEE Trans. Geosci. Remote Sens.*, vol. 49, no. 11, pp. 4239–4247, Nov. 2011.

[28] Y. Altmann, N. Dobigeon, S. McLaughlin, and J.-Y. Tourneret, "Residual component analysis of hyperspectral images - Application to joint nonlinear unmixing and nonlinearity detection," *IEEE Trans. Image Process.*, vol. 23, no. 5, pp. 2148–2158, June 2014.

[29] V. Mazet, S. Faisan, S. Awali, M.-A. Gaveau, and L. Poisson, "Unsupervised joint decomposition of a spectroscopic signal sequence," *Signal Process.*, vol. 109, pp. 193–205, April 2105.

[30] N. Dobigeon, S. Moussaoui, M. Coulon, J.-Y. Tourneret, and A. O. Hero, "Joint Bayesian endmember extraction and linear unmixing for hyperspectral imagery," *IEEE Trans. Signal Process.*, vol. 57, no. 11, pp. 4355–4368, Nov. 2009.

[31] E. J. Candès, X. Li, Y. Ma, and J. Wright, "Robust principal component analysis?" *Journal of ACM*, vol. 58, no. 1, pp. 1–37, 2009.

[32] J.-F. Giovannelli, "Ising field parameter estimation from incomplete and noisy data," in *Proc. IEEE Int. Conf. Image Processing (ICIP)*, Brussels, Belgium, Sept. 2011, pp. 1853–1856.

[33] N. Dobigeon and J.-Y. Tourneret, "Efficient sampling according to a multivariate Gaussian distribution truncated on a simplex," IRIT/ENSEEIHT/TéSA, France, Tech. Rep., March 2007. [Online]. Available: http://www.enseeih.fr/~dobigeon/papers/Dobigeon_TechReport_2007b.pdf

[34] Y. Altmann, S. McLaughlin, and N. Dobigeon, "Sampling from a multivariate Gaussian distribution truncated on a simplex: a review," in *Proc. IEEE-SP Workshop Stat. and Signal Processing (SSP)*, Gold Coast, Australia, July 2014, pp. 113–116.

[35] Y. Altmann, N. Dobigeon, and J.-Y. Tourneret, "Unsupervised post-nonlinear unmixing of hyperspectral images using a Hamiltonian Monte Carlo algorithm," *IEEE Trans. Image Process.*, vol. 23, no. 6, pp. 2663 – 2675, June 2014.

[36] A. Pakman and L. Paninski, "Exact Hamiltonian Monte Carlo for truncated multivariate Gaussians," *Journal of Computational and Graphical Statistics*, vol. 23, no. 2, pp. 518–542, 2014.

[37] Z. I. Botev, "The normal law under linear restrictions: Simulation and estimation via minimax tilting," *J. Roy. Stat. Soc. Ser. B*, vol. 78, no. 3, 2016, to appear.

[38] N. Chopin, "Fast simulation of truncated Gaussian distributions," *Statistics and Computing*, vol. 21, no. 2, pp. 275–288, 2011.

[39] L. Onsager, "A two-dimensional model with an order-disorder transition," *Phys. Rev.*, vol. 65, no. 3 & 4, pp. 117–149, Feb. 1944.

[40] J.-F. Giovannelli, "Estimation of the Ising field parameter thanks to the exact partition function," in *Proc. IEEE Int. Conf. Image Processing (ICIP)*, Hong-Kong, China, Sept. 2010, pp. 1441–1444.

[41] P.-A. Thouvenin, N. Dobigeon, and J.-Y. Tourneret, "Robust unmixing of multitemporal hyperspectral images – Complementary results and supporting material," University of Toulouse, IRIT/INP-ENSEEIHT, Tech. Rep., Sept. 2016. [Online]. Available: <http://thouvenin.perso.enseeih.fr/papers/Thouvenin2016submitted.pdf>

[42] A. Halimi, P. Honeine, M. Kharouf, C. Richard, and J.-Y. Tourneret, "Estimating the intrinsic dimension of hyperspectral images using a noise-whitened eigen-gap approach," *IEEE Trans. Geosci. Remote Sens.*, vol. 54, no. 7, pp. 3811–3821, July 2016.

[43] Y. Altmann, N. Dobigeon, J.-Y. Tourneret, and J. C. M. Bermudez, "A robust test for nonlinear mixture detection in hyperspectral images," in *Proc. IEEE Int. Conf. Acoust., Speech, and Signal Processing (ICASSP)*, Vancouver, Canada, June 2013, pp. 2149–2153.

Pierre-Antoine Thouvenin (S'15) received the state engineering degree in electrical engineering from ENSEEIHT, Toulouse, France, and the M.Sc. degree in signal processing from the National Polytechnic Institute of Toulouse (INP Toulouse), both in 2014. He is currently working toward the Ph.D. degree within the Signal and Communications Group of the IRIT Laboratory, Toulouse, France. His current research interests include statistical modeling, optimization techniques and hyperspectral unmixing.

Nicolas Dobigeon (S'05–SM'08–SM'13) received the state engineering degree in electrical engineering from ENSEEIHT, Toulouse, France, and the M.Sc. degree in signal processing from the National Polytechnic Institute of Toulouse (INP Toulouse), both in June 2004, as well as the Ph.D. degree and Habilitation à Diriger des Recherches in Signal Processing from the INP Toulouse in 2007 and 2012, respectively. He was a Post-Doctoral Research Associate with the Department of Electrical Engineering and Computer Science, University of Michigan, Ann Arbor, MI, USA, from 2007 to 2008.

Since 2008, he has been with the National Polytechnic Institute of Toulouse (INP-ENSEEIHT, University of Toulouse) where he is currently an Associate Professor. He conducts his research within the Signal and Communications Group of the IRIT Laboratory and he is also an affiliated faculty member of the Telecommunications for Space and Aeronautics (TéSA) cooperative laboratory. His current research interests include statistical signal and image processing, with a particular interest in Bayesian inverse problems with applications to remote sensing, biomedical imaging and genomics.

Jean-Yves Tourneret (SM'08) received the ingénieur degree in electrical engineering from the Ecole Nationale Supérieure d'Électronique, d'Electrotechnique, d'Informatique, d'Hydraulique et des Télécommunications (ENSEEIHT) de Toulouse in 1989 and the Ph.D. degree from the National Polytechnic Institute from Toulouse in 1992. He is currently a professor in the university of Toulouse (ENSEEIHT) and a member of the IRIT laboratory (UMR 5505 of the CNRS). His research activities are centered around statistical signal and image processing with a particular interest to Bayesian and Markov chain Monte-Carlo (MCMC) methods. He has been involved in the organization of several conferences including the European conference on signal processing EUSIPCO'02 (program chair), the international conference ICASSP'06 (plenaries), the statistical signal processing workshop SSP'12 (international liaisons), the International Workshop on Computational Advances in Multi-Sensor Adaptive Processing CAMSAP 2013 (local arrangements), the statistical signal processing workshop SSP'2014 (special sessions), the workshop on machine learning for signal processing MLSP'2014 (special sessions). He has been the general chair of the CIMI workshop on optimization and statistics in image processing hold in Toulouse in 2013 (with F. Malgouyres and D. Kouamé) and of the International Workshop on Computational Advances in Multi-Sensor Adaptive Processing CAMSAP 2015 (with P. Djuric). He has been a member of different technical committees including the Signal Processing Theory and Methods (SPTM) committee of the IEEE Signal Processing Society (2001-2007, 2010-present). He has been serving as an associate editor for the IEEE Transactions on Signal Processing (2008-2011, 2015-present) and for the EURASIP journal on Signal Processing (2013-present).